Experimental characterization of hot electron emission and shock dynamics in the context of the Shock Ignition Approach to Inertial Con finement Fusion

A Tentori, Arnaud Colaïtis, W. Theobald, A. Ruocco, Jocelain Trela, A. Casner, Edouard Le Bel, Raffestin D., S.A. A Pikuz, Koenig M., et al.

HAL Id: hal-03298927
https://cnrs.hal.science/hal-03298927

Submitted on 25 Jul 2021

Experimental characterization of hot electron emission and shock dynamics in the context of the Shock Ignition Approach to Inertial Confinement Fusion

A. Tentori[1],* A. Colatis[1], W. Theobald[2], A. Ruocco[1,6], J. Trela[1], A. Casner[1], E. Le Bel[1], D. Raffestin[1],
S.A. Pikuz[7], M. Koenig[3], B. Henderson[2], S. Baton[3], R. Betti[2,4,5], K. Anderson[2], M. Wei[2], and D. Batani[1]

[1]*Centre Lasers Intenses et Applications, CELIA,*
Université Bordeaux CEA-CNRS, UMR 5107, F-33405 Talence, France
[2]*Laboratory for Laser Energetics, University of Rochester, Rochester, NY 14623, USA*
[3]*Laboratoire pour lUtilisation des Lasers Intenses, LULI,*
CNRS-Ecole Polytechnique-CEA-Sorbonne Universités, UMR 7605, F-91128 Palaiseau, France
[4]*Department of Physics and Astronomy, University of Rochester, Rochester, NY 14623, USA*
[5]*Department of Mechanical Engineering, University of Rochester, Rochester, NY 14623, USA*
[6]*Central Laser Facility, STFC Rutherford Appleton Laboratory,*
Harwell Oxford, Didcot, Oxford OX11 0QX, United Kingdom and
[7]*Joint Institute for High Temperatures of Russian Academy of Sciences, 125412 Moscow, Russian Federation*
(Dated: March 18, 2021)

ABSTRACT

We report on planar target experiments conducted on the OMEGA-EP laser facility performed in the context of the Shock Ignition (SI) approach to inertial confinement fusion. The experiment aimed at characterizing the propagation of strong shock in matter and the generation of hot-electrons (HE), with laser parameters relevant to SI (1-ns UV laser beams with I $\sim 10^{16}$ W/cm^2). Time-resolved radiographies of targets were performed in order to study the hydrodynamic evolution.

The hot-electron source was characterized in terms of maxwellian temperature T_h and laser to hot-electron energy conversion efficiency η using data from different x-rays spectrometers. The post-processing of these data gives a range of possible values for T_h and η (i.e. $T_h[keV] \in [20,50]$ and $\eta \in [2\%,13\%]$). These values are used as input in hydrodynamic simulations to reproduce the results obtained in radiographies, thus constraining the range for the HE measurements. According to this procedure, we found that the laser converts $\sim 10\% \pm 4\%$ of energy into hot-electrons with T_h = 27 keV ± 7 keV. Such electrons have enough low temperature that they should not be a prehaeat concern in SI.

PACS numbers: 52.57.-z,52.38.-r,52.50.-b, 52.50.Jm

INTRODUCTION

Shock Ignition (SI) is an alternative approach to direct-drive Inertial Confinement Fusion which is based on the separation of the compression and the ignition phases. A low intensity laser pulse of $\sim 10^{14}$ W/cm^2 compresses the fuel, followed by an high-intensity ($\sim 10^{16}$ W/cm^2) 'spike'. This latter launches a strong converging shock at the end of the compression phase. The collision of this shock with the rebound compression shock raises the hotspot pressure creating the conditions to ignite the fuel [1] [2]. The high laser intensity required in the ignition phase exceeds the thresholds for the generation of different laser-plasma instabilities (LPI). These instabilities take place in the subcritical regions of the plasma, preventing part of the laser energy from arriving at the critical surface where more efficient absorption mechanisms can occur. Also large amounts of supra-thermal electrons are generated by the Electron Plasma Waves (EPW) created by Stimulated Raman Scattering (SRS) and Two-Plasmon Decay (TPD) [3] [4]. These hot-electrons (HE) can preheat the fuel making the compression more difficult or they can increase the hotspot mass ablating the shell and hence increasing the threshold for ignition [5]. On the other hand, recent publications predict an enhanced shock pressures from low temperature hot-electrons if their flux is sufficiently high [6]. As such, a critical step for answering the feasibility of shock ignition is the characterization in terms of energy and number of the hot-electron population understanding its effects on the hydrodynamics of the target. Although several experiments have addressed this point [7][8], we are still far from a complete comprehension of the problem, especially in conditions which are directly relevant for SI.

In this context we performed an experiment at the Omega-EP laser facility with the intensity range required for shock ignition. A UV (λ = 351 nm) laser of intensity of $\sim 10^{16}$ W/cm^2 was focused on a planar multilayer target producing a strong shock. Because of the absence of low-intensity pre-compression beams, the plasma scale lengths and the coronal electronic temperatures reached in this experiment are lower compared to real SI conditions. X-ray time-resolved radiographies allowed to study the shock propagation. In this configuration, a copious amount of hot-electrons is also produced and several diagnostics were used to characterize their temperature and intensity.

The paper is structured as follows: a description of the experimental setup and the involved diagnostics is given in the first part. Then we describe the post-processing

techniques of the spectrometer data and the coupling with hydrodynamic simulations done in order to characterize the electron beam. Finally, we discuss the evolution of hydrodynamic quantities considering the influence of electrons.

EXPERIMENTAL SETUP

The experiment was performed in the target chamber of the 4-beam OMEGA-EP laser facility [9] at the Laboratory for Laser Energetics. One or two high intensity UV interaction beams (B2, B4) ($\lambda = 351$ nm, 1.0 ns square pulse, beam energy of $\sim$1.25 kJ, $f/6.5$) irradiated a multi-layer target to produce a strong shock wave and copious amount of hot-electrons. The UV interaction beams were tightly focused on the target surface without phase plates to a focal spot size of $\sim$130 μm providing a nominal vacuum laser intensity of $\sim 1 \times 10^{16}$ W/cm^2 for one beam and $\sim 2 \times 10^{16}$ W/cm^2 for two beams. Planar targets consisted of two layers (175 or 250 μm CH/ 20 or 10 μm Cu) fabricated to 500 μm diameter disks. These were mounted on a 50 μm thick CH slab that inhibited hot-electron recirculation (see Fig. 1). The UV interaction lasers impinged on front of the 175 (or 250) μm thick CH layer at an angle of incidence of 23° with respect to the target normal. The Cu middle layer served as a tracer for hot-electrons emitting Cu K$_\alpha$ x-rays of 8.05 keV. Multiple x-ray diagnostics characterized the emission generated by the hot-electron population in order to obtain information on their energy spectrum.

The total yield of Cu K$_\alpha$ was measured by an absolutely calibrated Zinc von Hamos x-ray spectrometer (ZnVH) [10]. This spectrometer uses a curved HOPG crystal in von Hamos geometry to diagnose the x-ray spectrum in the range of $7 - 10$ keV. A high-spectral resolution x-ray spectrometer (HRS) used a spherically bent Si [220] crystal coupled to a charge-coupled device to measure the time-integrated x-ray emission in the 7.97- to 8.11-keV range [11]. The hot-electron-produced bremsstrahlung radiation was diagnosed by two time-integrating hard x-ray spectrometers (BMXSs) [12] at 25° and 65° off the target rear normal, respectively. The BMXSs are made by a stack of 15 image plate detectors with plastic and metal filters interleaved in-between. They can measure the x-rays in the range from 17 keV to 800 keV.

A streaked Sub-Aperture Backscattering Spectrometer (SABS) diagnosed the temporally resolved spectrum of the SRS backscattered light in B4 (430 nm 750 nm). However the total SRS reflected power could not be directly measured due to the small collecting area.

Two or three UV laser beams with a 3 ns square pulse irradiated a V foil target to produce a high flux of x-ray radiation at 5.2 keV, vanadium He$_\alpha$ line, used as source to perform time resolved radiographies (see Fig. 1). A to-
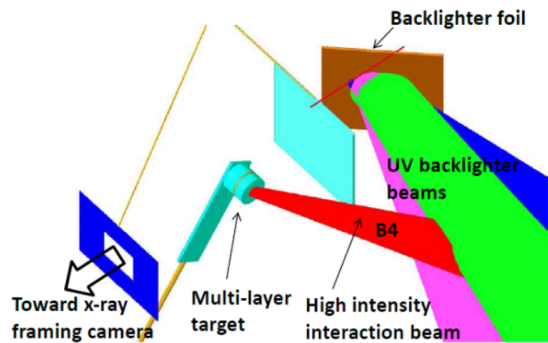

FIG. 1: Experimental setup for x-ray radiography. Two or three other UV beams irradiated a V foil and one high intensity UV beam interacted with the multi-layer target. An x-ray framing camera equipped with a pinhole array captured images of the shock front at various times.

tal energy of $\sim$5.0 kJ impinged on the V foil for the shots with two beams and $\sim$7.1 kJ to $\sim$7.5 kJ for shots with three beams. Two of the beams (B1, B3) were smoothed with SG8-0750 distributed phase plates (DPPs) [13]. The third beam (B2) did not use a DPP and was de-focused in order to match the spot size of the other two beams. The overlapped average intensity ranged from 3×10^{14} W/cm^2 to 5×10^{14} W/cm^2. A 50 μm thick CH heat shield placed between both targets absorbed the soft x-ray radiation from the V foil in order to prevent any premature x-ray preheat of the multi-layer target.

A four strip x-ray framing camera (XRFC) [14] equipped with an 4×4 array of 20-μm-diam. pinholes captured sixteen 2-D images of the shock front with $6 \times$ magnification at various times. The time and the spatial resolutions of the camera were $\sim$100 ps and $\sim$15 μm respectively.

Finally a 1-D time-resolved radiography was made using two perpendicular slits (6 mm x 90 μm and 10 μm x 90 μm) in front of the streak camera (PJX) [15]. The spatial resolution was about 10 μm and 40 ps of temporal resolution.

Tab. I presents a list of the performed shots considered in this paper, indicating the availability of experimental data from the diagnostics.

Shot Number	Ineraction beam on target	BMXS	ZNVH	Radiography	HRS
#28406	B4	Available	Available	2-D Not Exploitable	Available
#28407	B1	Available	Available	2-D Available	Available
#28410	B1+B4	Available	Not Available	2-D Not Exploitable	Available
#28412	B1	Available	Available	1-D Available	Available
#28415	B1+B4	Available	Available	1-D Not Exploitable	Available

TABLE I: Summary of performed shots. Shot number and the correspondent interaction laser beam focused on target are shown. The availability of experimental data coming from x-ray spectrometers and from radiography is indicated.

CHARACTERIZATION OF HOT-ELECTRONS

Here we present the methodology of analysis and post-processing of the BMXS and ZNVH data. The response of the spectrometers is analysed using Monte-Carlo simulations, providing a first estimation of the HE source. The results are then set as input in hydrodynamic simulations to reproduce the experimental behaviour observed in the radiography and refine the evaluation of the HE source.

I. Time-integrating hard x-ray spectrometer BMXS

The time-integrating hard x-ray spectrometer (BMXS) used in the experiment is composed of a stack of fifteen imaging plates (IP) of MS type [16], alternated by filters of different metals. The x-rays propagate into the stack creating a signal in the IPs according to their energy: higher energy photons propagate deeper in the stack. A schematic view of the filters disposition is shown in Fig. 2.

The whole stack is encapsulated in a cylindrical lead container in order to reduce the background signal, and a further 10 mm filter of politetrafluoroetilene $(C_2F_4)_n$ (PTFE, teflon) is placed in front of the stack to shielding it from plasma debris. In addition, this filter blocks low-energy photons coming from the coronal plasma and the copper K_α signal, while allowing higher energy photons produced by the propagation of hot-electrons in the target.
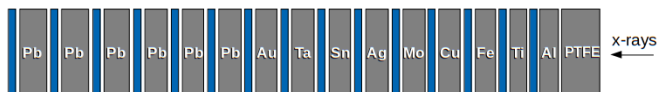

FIG. 2: Schematic disposition of the filters (in grey) and imaging plates (in blue). X-rays are penetrating the stack from the right.

After recording the signal, the imaging plates are read in a dedicated scanner which induces Photo Stimulated Luminescence (PSL). Fig. 3 shows the signal recorded in shot #28407. In general all the shots had signal up to the seventh or eighth IP. The background noise is around 1% of the signal of the seventh IP and it does not influence the measure. The PSL value is related to the absorbed dose by a calibration curve [17].
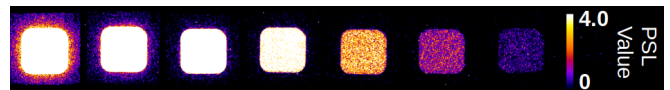

FIG. 3: Example signals obtained in the IP stack for shot #28407.

To extract the x-ray spectrum which led to a given energy deposition, one must first characterize the response of each IP inside the BMXS to a monochromatic x-ray beam. This is calculated by performing MC simulations in which the 3D detector geometry is reproduced. The simulations were performed with the Geant4 MC code [18] using the physics library Penelope [19]. Here we used 46 logarithmically spaced photon spectral bins from 5 keV to 1 MeV in order to calculate the deposited energy per photon $D_i(k)$, in the k-th IP for the i-th energy bin. Results are shown in Fig. 4.
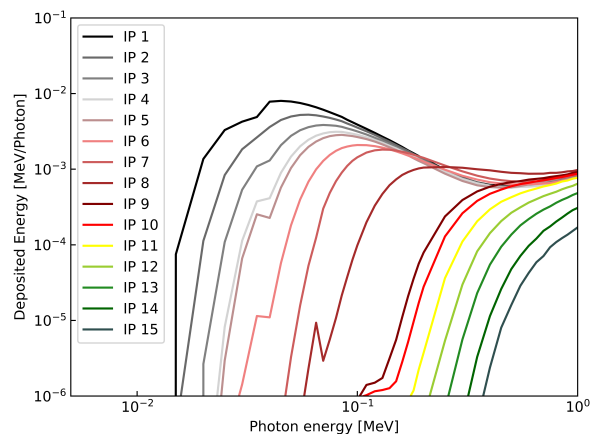

FIG. 4: Response curves of each IP in the BMXS spectrometer calculated using MC simulations.

For a generic photon distribution function $f_{\rm ph}(E)$ it is

possible to calculate the energy deposition E_t in the k-th IP using to the formula:

$$E_t(k) = \sum_{i=1}^{45} \int_{E_{i-1}}^{E_i} f_{ph}(E) \frac{D_i(k) + D_{i+1}(k)}{2} dE. \quad (1)$$

Considering the decaying behaviour of the signal through the IPs, we chose an exponential photon distribution function of the type $f_{ph}(A_{ph}, T_{ph}, E) = \frac{A_{ph}}{E} e^{-E/T_{ph}}$ with free parameters A_{ph} and T_{ph}. The choice of this type of $f_{ph}(E)$ is related to the fact that, as remarked later, this is the shape of photon distribution function produced on the detector by a 2-D electron maxwellian distribution function that propagates inside the target. Furthermore, theoretical studies predict that this kind of curves corresponds to the photon distribution function produced by a 3-D electron maxwellian that propagate in an infinite homogeneous plasma [20]. The values of the free parameters A_{ph} and T_{ph} are found fitting the experimental data by performing a reduced χ^2 test. The latter reads:

$$\chi^2 = \frac{1}{\nu} \sum_{k=1}^{N_{ip}} \frac{(E_t(k) - E_{exp}(k))^2}{\sigma_{exp}^2(k)} \rightarrow 1, \quad (2)$$

where $E_t(k)$ is the calculated deposited energy, $E_{exp}(k)$ the experimental one, σ_{exp}^2 the variance of the experimental value and ν is the number of degrees of freedom. Fig. 5 shows the ensemble of possible values for parameters A_{ph} and T_{ph} that lead to $\chi^2 \rightarrow 1$ for the two spectrometers, for shot #28407. In general a good agreement between the two spectrometers was observed for all shots.
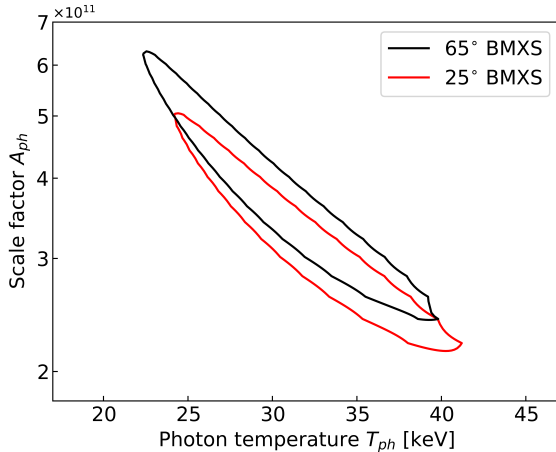

FIG. 5: Contours of parameters A_{ph} and T_{ph} leading to a reduced χ^2 of 1 in the post processing of data from the two BMXS, for shot #28407. Results for the spectrometers placed at 25° and 65° are given in red and black respectively.

II. K_α spectrometers

The two K_α spectrometers, the ZNVH and the HRS, are based on the same working principle: a crystal deviates the K_α x-ray on the sensitive part of the detector. In the ZNVH a passive detection system is used, the imaging plate, while the HRS uses a streak camera. Knowing the calibration of the spectrometers, it is possible to reconstruct the x-ray spectrum detected. Fig. 6 shows the signal detected by the ZNVH for the shot #28407, after a correction by the background. In the figure it is possible to appreciate how the Cu K_α peak is well resolved by the diagnostic. The integral of the peak gives the total number of K_α photon per steradian that reached the instrument.
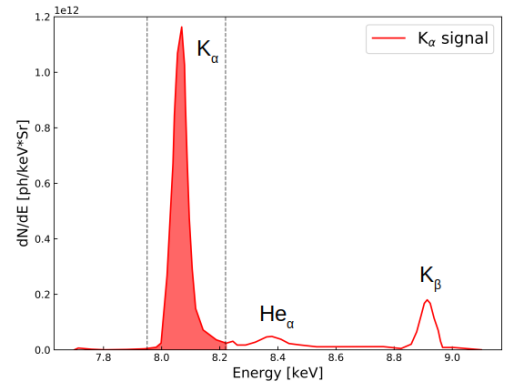

FIG. 6: X-ray spectrum detected by the ZNVH spectrometer for the shot #28407, after the background correction.

Since as shown by Fig. 7 the two spectrometers gave a coherent response, in the continuation of our analysis we will consider only the data from the ZNVH.
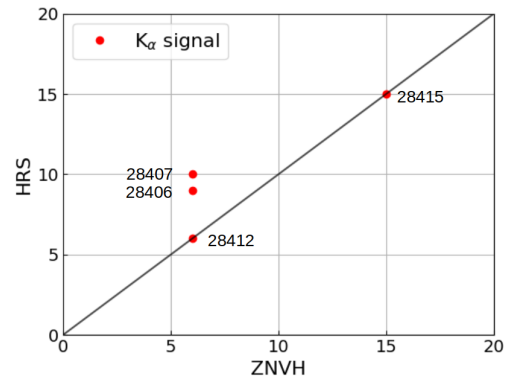

FIG. 7: Ratio between the signal detected by the HRS and ZNVH. The two spectrometers gave a coherent response.

III. Post-processing of the BMXS and ZNVH

Information on the hot-electron population is inferred by simulating the propagation of the hot-electron beam in the target and finding the parameters that reproduce both the bremsstrahlung emission and the K_α signal detected by the diagnostics. These simulations are performed with Geant4, which allows for a detailed description of the electrons' collision in matter and x-ray emission. Unfortunately the code does not account for the hydrodynamic evolution of the target and the collective effects, but these are playing a minor role in determining the x-ray emission due to electrons' propagation. For sufficiently large laser spot, the 1D assumption that the product $\rho < l >$ is the same for cold and for ablated target holds, where $< l >$ is the target length for the two cases. Hence, at first order, electrons should lose a similar amount of energy crossing a cold target or the real irradiated one.

While the geometry and composition of targets are fully described in the simulation, reproducing the exact position and geometry of the detectors would require significant computational resources in order to achieve acceptable statistics. Indeed, the spectrometers were mounted on the chamber wall at 1.8 meters from TCC. For these reasons, the detectors in the MC simulation are represented by spherical coronas at the correct angle and distance. This approach improves statistics, but assumes cylindrical symmetry (See Fig. 8).
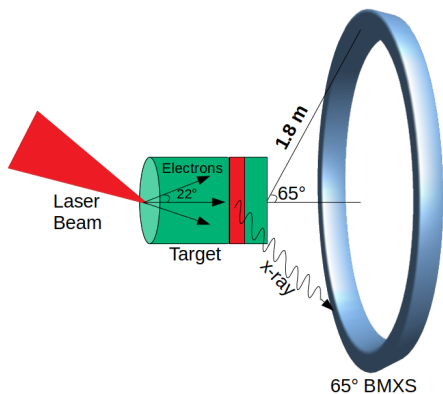

FIG. 8: Schematic illustration of target and detector configuration set in Geant4 simulation.

The electron beam with a size of 100 μm is injected from the front side of the target where the laser impinges. Various cases are considered concerning the beam initialization : $\pm 45°$ or $\pm 22°$ of initial divergence and of $0°$ or $23°$ of inclination with the respect to target normal. Bremsstrahlung and K_α generation were simulated using the physics libraries Penelope and Livermore [21]. Simulations were conducted by launching 22 monochromatic beams with logarithmic-spaced

energies from 5 keV up to 300 keV. The 2D Maxwellian $f_e(N_e, T_h, E) = \frac{N_e}{T_h}e^{-E/T_h}$ that reproduces both the bremsstrahlung spectrum $f_{ph}(E)$ on the BMXS and the K_α signal on the ZNVH is then reconstructed. In the function, N_e represents the total number of electrons and T_h the temperature.

The post-processing of the BMXSs showed that there are several combinations of possible values for the parameters A_{ph} and T_{ph} that can reproduce the measurements. Because of this, we consider three representative points for each BMXS (see Fig. 9): the two extreme points (f_{ph1} and f_{ph3}) and the central point (f_{ph2}).
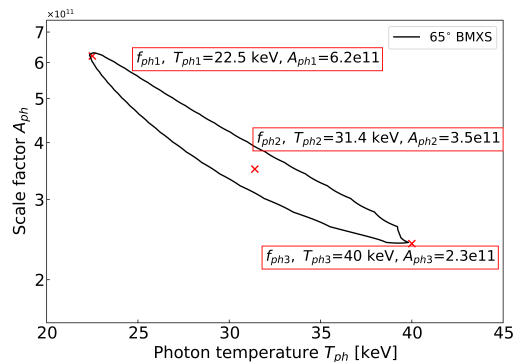

FIG. 9: Contours of parameters A_{ph} and T_{ph} leading to a reduced χ^2 of 1 in the post processing of the BMXS placed at $65°$ for the shot #28407. The three representative points with the corresponding values of A_{ph} and T_{ph} are indicated.

Since no significant differences were observed between the two physics libraries in the simulation of the bremsstrahlung radiation, only the results from Penelope are shown. Tab. II shows the electron distribution functions $f_e(N_e, T_h, E)$ that generate the three photon distributions $f_{ph}(E)$ on the $65°$ BMXS for shot #28407. As can be observed, there are no remarkable differences between different initial divergences and inclinations of the input electron beam. The low mean kinetic energy of electrons leads to severe large-angle scattering that causes the particles to lose their directionality. This strengthens the initial assumption of cylindrical symmetry. As an example, Fig. 10 compares $f_{ph1}(E)$ and the simulated bremsstrahlung spectra produced on the $65°$ BMXS using the $f_{e1}(E)$. For these particular target configurations and energy ranges, the photon distribution produced by an exponential distribution function of electrons has the form of $f_{ph}(E) = \frac{A_{ph}}{E}e^{-E/T_{ph}}$. This justifies the initial choice of fitting the BMXS signal with these kind of functions (see Sec. I).

Across all shots, it is possible to observe an average electron temperature T_h that spans from 20 keV up to

Electron spectra $f_e(E)$							
		$f_{e1} \to f_{ph1}$		$f_{e2} \to f_{ph2}$		$f_{e3} \to f_{ph3}$	
Initial divergence	Beam incidence	N_{e1} [10^{16}]	T_{h1} [keV]	N_{e2} [10^{16}]	T_{h2} [keV]	N_{e3} [10^{16}]	T_{h3} [keV]
22°	0°	5.1	21	1.6	29	0.6	39
45°	0°	4.9	21	1.6	30	0.6	40
22°	23°	5.1	21	1.6	30	0.6	40
45°	23°	5.1	21	1.6	30	0.6	41

TABLE II: Coefficients N_e and T_h of the electron distribution functions $f_e(E)$ that generate the three $f_{ph}(E)$ detected by the 65° BMXS, for shot #28407, for all the possible combinations of initial beam divergences and incidences.
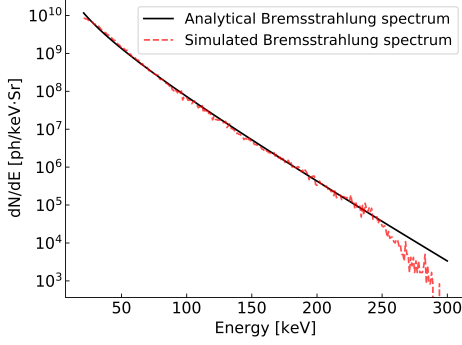

FIG. 10: Comparison of the bremsstrahlung spectra $f_{ph1}(E)$ in black and simulated one resulting from $f_{e1}(E)$ reported in Tab. II in red. The bremsstrahlung spectra comes from the post-processing of the 65° BMXS for the shot #28407.

45 keV, with absolute number of electrons N_e ranging from $6 \cdot 10^{15}$ up to $5 \cdot 10^{16}$.

Concerning the K_α simulations, similarly to the generation of the bremsstrahlung spectrum, the initial configurations of the electron beam is not seen to influence the K_α emission. Therefore, only results from the simulations with $\pm 22°$ initial divergence and at normal incidence beam are reported. Fig. 11 shows possible values N_e and T_h that reproduce the K_α signal on the ZNVH, combined with the values obtained previously by the BMXS, for the shots #28406 and #28407. A disagreement of about 25% is found between the libraries Livermore and Penelope in reproducing the K_α. Since they predict that the same amount of electrons reaches the copper with identical energy distribution, the discrepancy must be attributed to differences in the computation of the cross section for the K-shell ionization $\sigma_k(E)$. These differences are however comparable to the relative standard deviation of the experimental measures of $\sigma_k(E)$ [22].

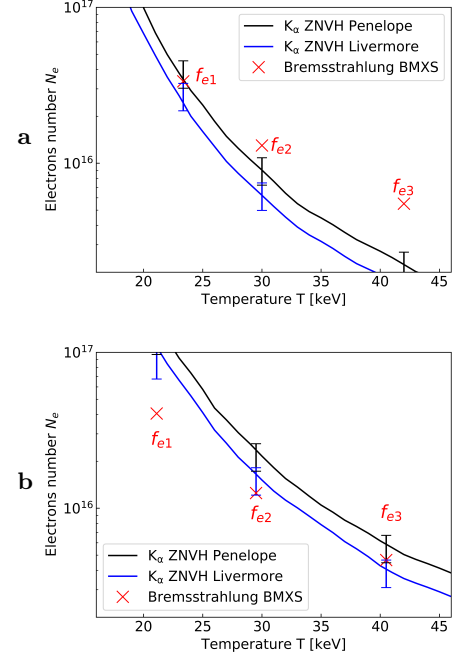The disagreement between the results considering

FIG. 11: Map of possible values of N_e and T_h that can reproduce the experimental data (K_α and bremsstrahlung spectrum) for shots #28406 (a) and #28407 (b). The black and the blue lines result from K_α simulations with libraries Penelope and Livermore, respectively. The red crosses indicate the average values coming from the two BMXS, using the three representative points scheme. The experimental error on the K_α signal, evaluated to be around 20%, is shown by error-bars.

different shots does not allow to reduce the ranges of N_e and T_h. It is thus necessary to keep the scheme of three representative points. Figure 12 illustrates the conversion efficiency of laser energy into hot-electron energy for the five shots, considering for each the three possible f_e. Points in between are chosen in case of significant discrepancies between the response of the BMXS and ZNVH (Fig. 11). In shots using a single

interaction beam, three main regions can be identified: from 20 keV to 26 keV with efficiencies around 10%, from 27 keV to 35 keV with efficiencies around 5% and from 36 keV up to 45 keV with efficiencies around 2%. The shots performed with two laser beams show similar conversion efficiencies and slightly higher temperatures. In order to discriminate between the three regions, we use all these values as input of hydrodynamic simulations and we evaluate which reproduces the experimental evolution seen in the radiographies.
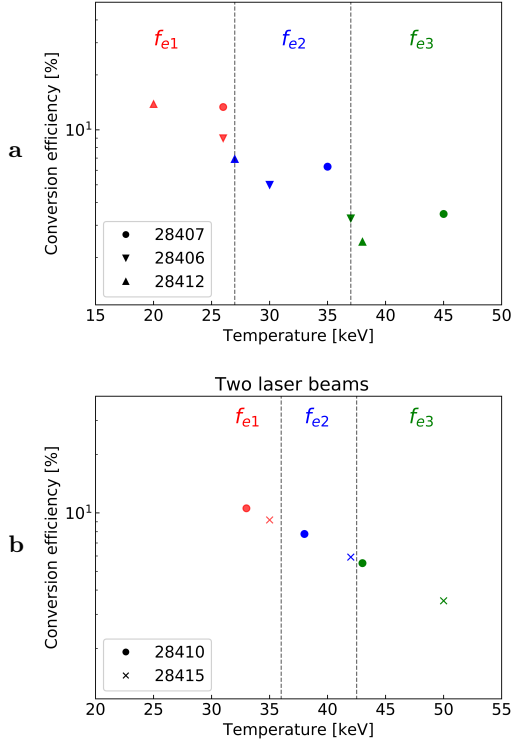

FIG. 12: Laser to hot-electron conversion efficiency as a function of temperature. Fig. **a** reports the shots in which one beam was focused on target (1250 J): #28406, #28407, #28412. Fig. **b** reports shots #28410 and #28415 with two laser beams (2500 J). The three main areas, corresponding to the three $f_e(E)$ detected by the BMXS and ZNVH, are reported in red, blue and green for each shot, respectively.

HYDRODYNAMIC EVOLUTION OF TARGET AND EFFECT OF HOT ELECTRONS

I. Time-resolved radiographies

The shock propagation in the target was monitored by x-ray radiographies taken at different times. Fig. 13 shows the array of sixteen radiographies captured by the XRFC for the shot #28407.
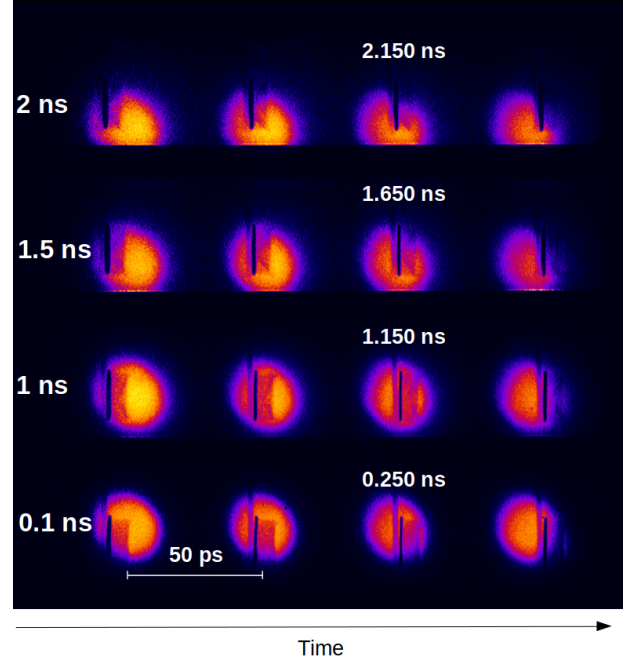

FIG. 13: Array of 2-D radiographies captured at various times by the XRFC for shot #28407. Between each image on the line there are 50 ps.

Among these, Fig. 14 shows the radiography at 250 ps and at 1.150 ns. At 250 ps, when the target is still cold, it is possible to see the CH ablator of 175 μm thickness, the copper plate of 20 μm, the plastic holder of 50 μm and a ~ 15 μm of glue between the holder and the copper. This indicates a correct alignment of the XRFC and a low value of parallax for the images of the third column of the array. In the radiography at 1.150 ns it is possible to discern the shock that propagates inside the ablator, although the poor contrast of the image makes the precise measurement of its position difficult. It is however clearly possible to see that the copper layer is thicker. Since at this time the shock did not reach the layer, such expansion has been attributed to the effect of HE.
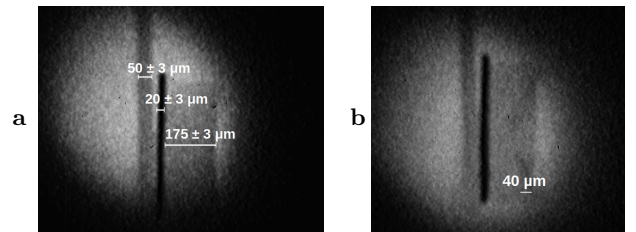

FIG. 14: Radiography of the target at 250 ps (a) and at 1.150 ns (b) for shot #28407. In the radiography (a) the thickness of the ablator, copper plate and holder are indicated. Laser impinges on the right.

The shock position and the copper plate expansion are the figures of merit considered to characterize the hot-electron source. Different intensities and kinetic energies of the hot-electron beam will strongly affect the variation in time of these two quantities. The expansion of the plate is evaluated by referring to transmissivity profiles taken along the cylinder axis, as shown in Fig. 15. The minimum in the curves indicates the presence of the copper and the FWHM represents its thickness. The transmissivity values were then normalized by the values resulting from the plastic holder. The holder remains uncompressed during the radiography, and we can hence assume that the x-ray flux that goes through it is constant and proportional to the backlighter emission.
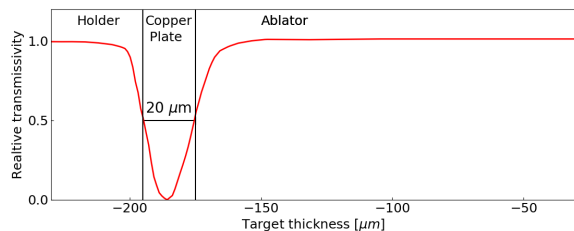

FIG. 15: Transmissivity profile on the cylinder axis extracted from the radiography at 250 ps for shot #28407. The position of ablator, copper plate and holder are indicated in the figure. The thickness of copper is measured by the FWHM of the transmissivity profile.

II. Hydrodynamic simulations

Hydrodynamic simulations were performed with the 2D Hydrodynamic Code (CHIC) [23] developed at CELIA. The code describes single fluid two-temperatures hydrodynamics with thermal coupling between electrons and ions. Electron heat transport is described by the Spitzer-Harm model with flux limiter, while radiation transport is described by a multi-group approach using tabulated opacities. The calculation of hydrodynamic quantities relies on equations of state taken from the SESAME database, and the ionization is calculated according the Thomas-Fermi theory. The laser propagation is modelled using ray tracing accounting for inverse bremsstrahlung absorption. Losses due to Stimulated-Brillouin Scattering (SBS) are not modelled by such simple approaches. Since in our experiment the SBS reflected power was not directly measured, the experimental shape of the pulse was corrected by the amount of SBS evaluated by performing simulations with the time-enveloped wave solver LPSE [24]. This code couples the equations that describe the pump wave with the equations for the Raman and Brillouin scattered light and plasma waves. Plasma waves equations are solved around a given plasma frequency ω_{pe0}, whereas the Raman scattered field is enveloped at $\omega_r = \omega_0 - \omega_{pe0}$. The fluid equations for the plasma density and velocity govern the plasma dynamics. Coronal plasma density, velocity profiles and electron temperatures at quarter critical density were extracted from an initial CHIC simulation with the experimental base pulse at four times: 0.3 ns, 0.5 ns, 0.9 ns and 1.3 ns. These parameters are then used as input for LPSE to calculate the percentage of SBS reflected light and study the Raman scattering at quarter critical density in one-dimensional geometry. The LPSE simulations run for 25 ps, which is long enough to observe the saturation of Raman and Brillouin instabilities. Discussion on the results of such simulations lies beyond the purpose of this work. Here, we only retain the fraction of the Brillouin back-scattered light when the saturation of the instability is reached. The amount of the Brillouin reflected light obtained in the four simulations is the 2%, 7%, 46% and 2% of the incoming pump wave, respectively. The correction is done by interpolating linearly in time these percentages and subtracting the values to the base pulse. The total fraction of scattered power in the simulation is around 20%. The shapes of experimental (red line) and the SBS-corrected (orange line) pulses are shown in Fig. 17.
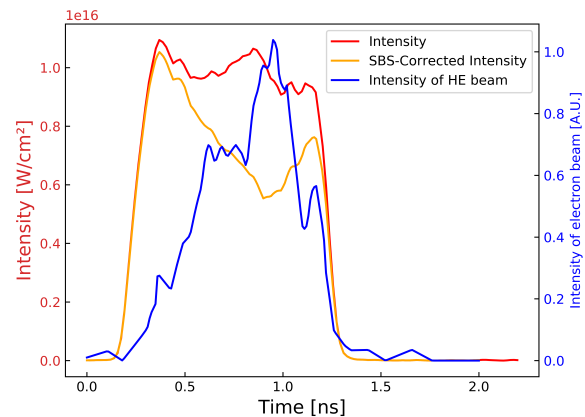

FIG. 17: Experimental laser pulse shape (red) and SBS-corrected laser pulse shape (orange). The intensity of HE beam (shown in blue) is assumed to exactly follow the SRS reflected power measured by the SABS, as shown in Fig 16. Data are referred to shot #28407.

Hot-electron propagation in the hydrodynamic simulation is modelled using the hot-electron transport package implemented in CHIC [25]. Electrons propagate along straight lines depositing energy into the mesh according to the plasma stopping power formulas [26] [27]. Straggling and blooming of the beam are taken into account
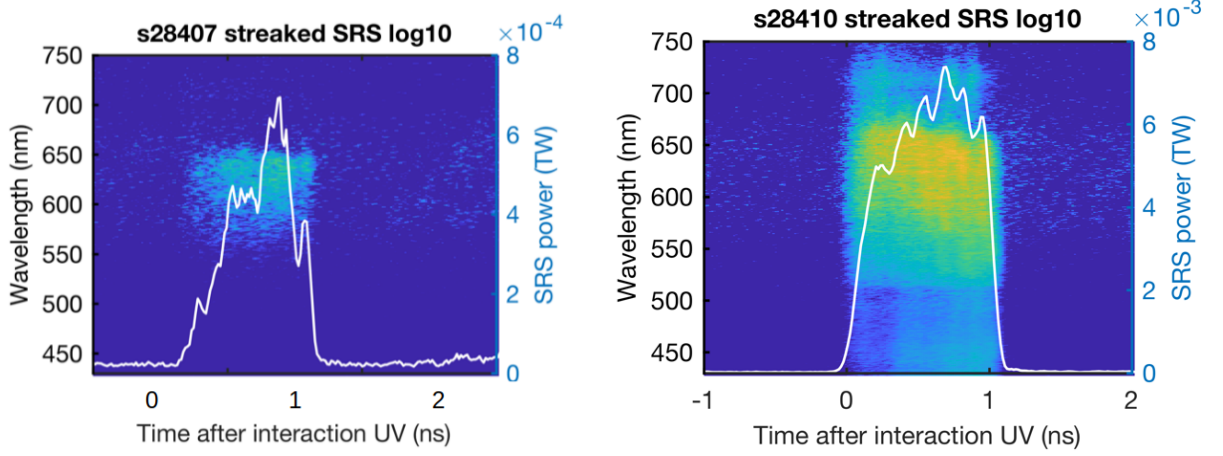
FIG. 16: Reflected light due to SRS and TPD collected by the SABS for shot #28407 and #28410. The bandwidth of the diagnostic ranges from 400 nm up to 750 nm. The temporal profile of the signal is indicated by the white line. The values of the SRS power collected are not significative, since the diagnostic covers only the 6% of the beam solid angle.

by using the Lewis' model [28]. Electrons are described by a 2D maxwellian function $f_e(N_e, T_h, E) = \frac{N_e}{T_h} e^{-E/T_h}$ in which the parameters N_e and T_h are taken from experimental data. The parameter N_e is related to laser-HE conversion efficiency η (See sec II.). This coefficient and the position where the HE source is initialized are modelled using the signal obtained by the SABS, as explained following. As shown by Fig. 16, this diagnostic detects light generated by absolute and convective SRS and the $\omega/2$ TPD signal. From Fig. 16 it is possible to see that the strongest signal is the broad spectral features characteristics of convective SRS, while the $\omega/2$ signal produced by TPD is weaker. The centers of the convective SRS emissions are around 625 nm and 575 nm for shots #28407 and #28410 respectively. According to the relation between the wavelength of backward scattered SRS and the density at which the scattering occurs [29]

$$\lambda_{\mathrm{SRS}} = \lambda_{\mathrm{L}} \left[1 - \sqrt{\frac{n_e}{n_c} \left(1 + 3k^2 \lambda_{\mathrm{D}}^2 \right)} \right]^{-1}, \qquad (3)$$

we can estimated that the average SRS emission happens at $0.14 n_c$ - $0.18 n_c$. In the simulations, electron beamlets are thus initialized at $0.14 n_c$ with an initial divergence of $\pm 22°$. This approach does not consider electrons generated at n_c, mainly produced by resonant absorption (RA). This is justified considering that the temperature of RA electrons is estimated to be ~ 9 keV, according to the the scaling law [30]

$$T_{RA}^h = 1.58 \cdot 10^{-3} \left(I \lambda^2 \right)^{0.25} \ \mathrm{keV}, \quad I\lambda^2 \in \left[10^{15}, 10^{17} \right], \tag{4}$$

where I is in W/cm^2 and λ is in μm. Considering the range of electron temperatures found by the spectrometers (20 keV - 50 keV, see Sec. II), the bremsstrahlung

and the K_α signals produced by RA electrons on the BMXS and ZNVH are negligible compared to the signals produced by SRS and TPD electrons. Furthermore, simulations are not sensitive to small variations in the initial position of beamlets, because of their low initial divergence and considering the fact that electrons propagating in the corona do not lose much energy. The intensity of the electron beam is modelled in time considering the conversion efficiency $\eta(t)$ that follows temporally the signal measured by the SABS, as shown in Fig. 17. However, the SABS instrument only covers 6% of the beam solid angle, contrary to the FABS used in NIF and OMEGA60. Because of this, the total energy measured was only the 0.02% of the incident light. To model $\eta(t)$, it is thus necessary to renormalise and rescale the SABS signal considering the conversion efficiency given by BMXS and ZNVH (10%, 5%, 2%, see Sec. II).

Three different CHIC simulations are performed in order to determine which combination of conversion efficiency η and average temperature T_h better reproduces the experimental behaviour. The three corresponding $f_e(E)$ are reported in Tab. III.

	f_e		
	T_h [keV]	η [%]	$N_e[10^{16}]$
$f_{e1}(E)$	26	10	5
$f_{e2}(E)$	35	5	1.44
$f_{e3}(E)$	45	2	0.6

TABLE III: Parameters of maxwellian functions $f_e(E)$ obtained from the post-process of BMXS and ZNVH for the shot #28407, used as input in CHIC.

III. Comparison between experimental and synthetic radiographies

The generation of synthetic radiographies from simulations is accomplished by reproducing the 3D cylindrical density profiles and then by calculating the theoretical transmissivity maps at the times of interest, according to the formula:

$$T(t, x, y) = \exp\left[-\left(\frac{\mu}{\rho}\right)\int\rho(z)\mathrm{d}z\right]. \qquad (5)$$

In the latter $\rho(z)$ is the density of the material along the radiography axis and $\frac{\mu}{\rho}$ is the mass absorption coefficient in plastic and copper [31]. The images are then blurred with a 2D Gaussian convolution with standard deviation of 15 μm to take in account the spatial resolution of the pinhole array. Transmissivity profiles are then extrapolated along the cylinder axis to evaluate the copper plate expansion. The values are renormalized by the transmissivity of the holder to be consistent with the experimental analysis.

To retrieve information on the hot-electron beam we rely on the radiography taken at 1.650 ns, when the laser interaction is finished and hot-electrons have already deposited their energy in the target. At this time, the hydrodynamic evolution is only influenced by the electrons pre-heat and the shock is approaching the copper that expands significantly. The experimental thickness, evaluated from the transmissivity curves, is 34 ±3 μm. Considering a diagnostic temporal resolution of ±50 ps, Fig. 18 shows the superposition between the experimental curve at 1.650 ns and the theoretical ones for a time windows that spans from 1.600 ns up to 1.700 ns. Three hot-electrons cases (denoted with the corresponding f_{e_i}) and the case without hot-electrons (woHE) are reported. The decrease of the synthetic transmissivity in the ablator is due to the presence of the shock that compresses matter. This effect allows to see the shock front propagating in the ablator in the cases f_{e_3} and woHE, while in the other two cases the shock has already reached the copper plate at 1.650 ns. In the experimental curves this behaviour is not observed and, on the contrary, the values coming from the compressed ablator are slightly higher compared to ones coming from the un-compressed holder. This is possibly due to non-uniformities in x-ray beam generated by the backlighter. While this issue makes the precise detection of the shock position difficult, it does not affect the information related to the copper thickness. From Fig. 18 it is possible to observe that the low temperature HE distributions (f_{e_1}, f_{e_2}) reproduce an expansion of the plate that approaches the experimental behaviour. For the other cases (f_{e_3}, woHE), a similar expansion would be obtained only at larger observation time ($\geq$ 100 ps), which is not compatible with the resolution of
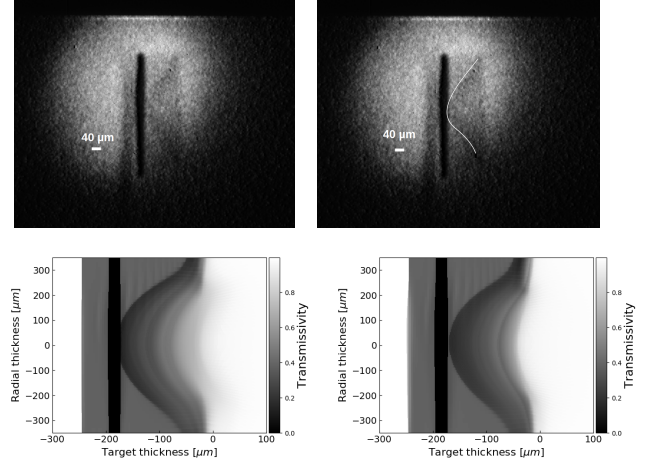
the instrument.

FIG. 19: [Top] Experimental radiography of shot #28407 at 1.650 ns. In [Top-Right] the shock front is highlighted; [Bottom-left] synthetic radiography obtained by the simulation with $f_{e1}(E)$ at t= 1.700 ns; [Bottom-right] synthetic radiography obtained by the simulation with $f_{e2}(E)$ at t= 1.700 ns.

The experimental radiography at 1.650 ns is illustrated in Fig 19. At that time the shock front is into the copper plate. We report in the same figure the synthetic radiographies obtained from the simulations with $f_{e1}(E)$ and $f_{e2}(E)$ at 1.700 ns, considering as before the limit in the time resolution of the camera. In the case $f_{e2}(E)$ the shock is approaching the plate, while in the simulation with $f_{e1}(E)$ the shock is already propagating inside, in agreement with the experimental behaviour. In the other two cases (without HE and $f_{e3}(E)$) the shock at 1.700 ns has not yet reached the plate. As such, the 2D x-ray radiography suggests that the HE distributions $f_{e1}(E)$ and $f_{e2}(E)$ are more consistent with the experimental results.

The conclusions presented from the time-gated radiography are strengthened by results from the 1-D time-resolved radiography, shown in Fig. 20 for shot #28412. This figure shows the ablator of 175 μm, the ablation zone that grows in time and the copper plate. The progression of the shock into the target is indicated by the white-dashed line in Fig. 21, in which we compare the experimental radiography with the synthetic ones.
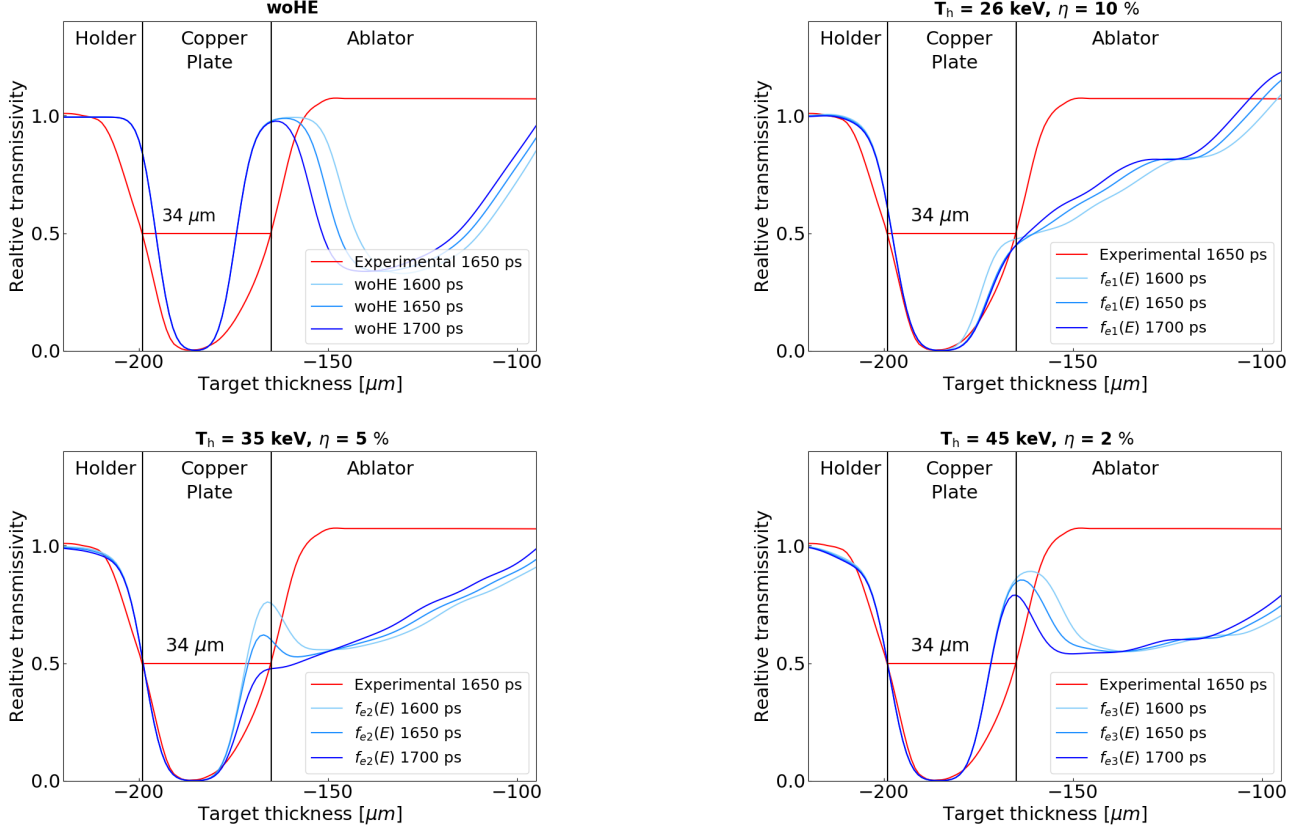
FIG. 18: Transmissivity curves taken along the central axis. In red the experimental curve extracted from the radiography at 1.650 ns for shot #28407, in blue the synthetic curves for time window that spans from 1.600 ns up to 1.700 ns. The four figures correspond to the four simulated cases: [top-left] case without HE; [top-right] simulation with hot-electron beam $f_{e1}(E)$; [bottom-left] simulation with hot-electron beam $f_{e2}(E)$; [bottom-right] simulation with hot-electron beam $f_{e3}(E)$.
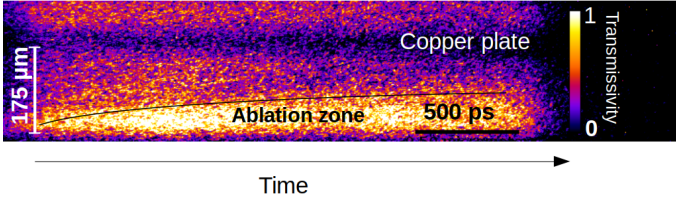

FIG. 20: Experimental time resolved 1D radiography in the shot #28412. Time is on the x axis. Laser impinges from the bottom.

Despite the large error bars due to low contrast of the experimental image, there is an indication that lower temperatures and higher efficiencies are more appropriate to reproduce the experimental behaviour.

In conclusion, the simulation with the HE distribution $f_{e1}(E)$ is better in agreement with experimental results, either considering the 2-D radiography and the 1-D time resolved radiography. The behaviour predicted by the simulation with $f_{e2}(E)$ approaches the experimental results, while the simulations with $f_{e3}(E)$ and without HE

beam are clearly not in agreement with experiment. As such, for shots with one laser beam, we identify an hot-electron temperature $T_h = 27$ keV ± 7 keV and a conversion efficiency $\eta = 10\% \pm 4\%$. For the shots in which two laser beams were used, the unavailability of exploitable radiographies does not allow to retrieve detailed information on the hot-electron beam.

IV. Temperature of the copper plate

The K_α spectra measured by the HRS are used to estimate the electronic temperature reached by copper during the irradiation. The spectrum measured by the HRS for shot #28407 is shown in Fig. 22 (red line). In the figure it is possible to see the two peaks related to the de-excitation of the copper K_α, namely $K_\alpha 1$ and $K_\alpha 2$, resolved by the instrument. The emission lines, in the case of cold material, are at 8.0478 keV for $K_\alpha 1$ and at 8.0278 keV for $K_\alpha 2$. The heating and the consequent ionization of the material due to the presence of hot-electrons in-
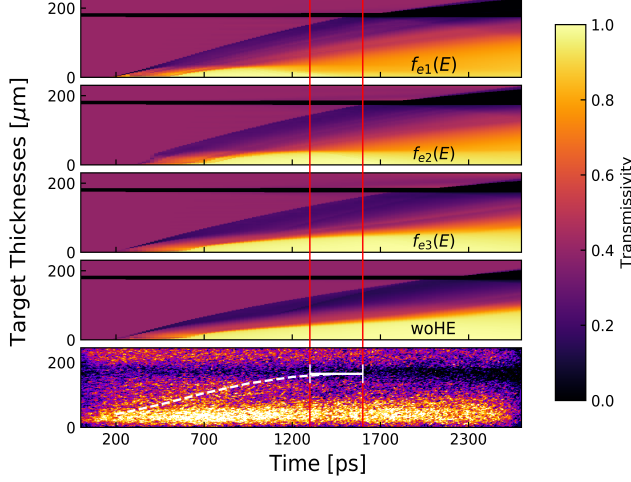
FIG. 21: Comparison between the experimental 1D time resolved radiography of shot #28412 and the synthetic ones. The three hot-electron cases (denoted f_{e_i}) and the without HE (woHE) case are reported. The time at which the shock arrives on the plate is marked with red lines. The white dashed line indicates the progression of the shock.

FIG. 22: Experimental and synthetic K_α spectra superimposed. The experimental signal in red refers to the shot #28407. The synthetic signal are reproduced considering electronic copper temperatures between 10 eV (blue curve) and 30 eV (black curve).

duces a wavelength shift of the emission that results in broadening of the peaks [32]. Since the position of the HRS pointed to the front side of the target, the measured temperatures are referred to the first layers of the plate. This is because the K_α signal coming from those layers is stronger and less attenuated by the target itself. The experimental broadening is compared with synthetic signals simulated using the PrismSpect code [33]. These synthetic signals are reproduced considering the emission of K_α at different copper temperatures.

As shown in Fig. 22, the broadening of the peaks indicates temperatures greater than 10 eV, but lower than 30 eV. The copper temperature computed by CHIC for simulations with HE presents its maximum of 13 eV in the first part of the plate, decreasing down to 5 eV in the rear side. The values provided by the simulation without HE are 0.2 eV. The values predicted by the simulations with hot-electrons are thus in much better agreement with the experimental results.
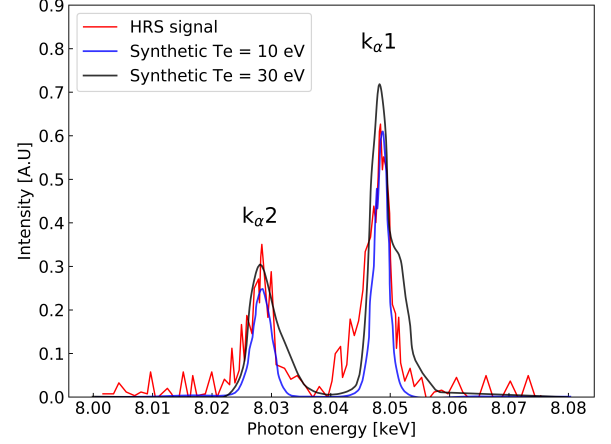
INFLUENCE OF HOT-ELECTRONS ON THE HYDRODYNAMIC AND DISCUSSION

We now analyse the simulation results that matches the experimental data. As explained in the previous section, the laser pulse used as input in the simulations follows temporally the experimental pulse, after a correction taking into account the SBS reflection. Hot-electrons are generated at $0.14n_c$ following the temporal profile of the backscatterd light measured by the SABS instrument. HE beams are energetically described by exponential distributions characterized by $T_h = 26$ keV and $\eta = 10\%$.

Plasma Parameters

The $n_c/4$ density-scale length rises up to 150 μm in the first 0.8 ns, while the $n_c/4$ coronal electronic temperature reaches ~ 2.1 keV in the first 0.6 ns, as shown in Fig. 23. Considering the temporal evolution of these parameters, the intensity threshold for SRS [34] and TPD [30] are exceeded after ~ 200 ps, i.e. almost at the begin of the drive laser pulse.
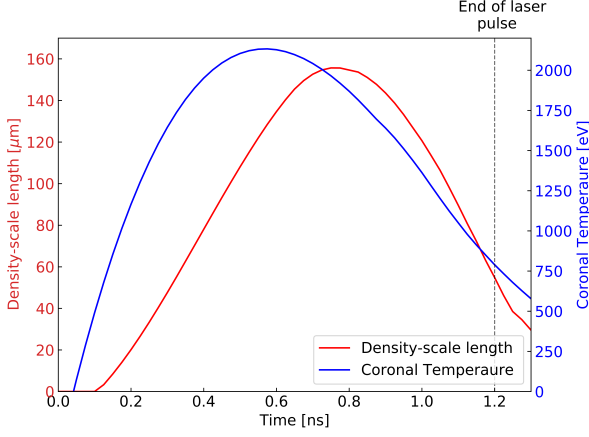
FIG. 23: Evolution in time of the density-scale length and coronal electronic temperature computed at $n_c/4$. The time interval considered corresponds to the time of SRS activity observed in the SABS.

Comparison with similar SI experiments

Compared with a recent shock ignition experiment carried out in OMEGA [35], our analysis shows similar hot-electron temperature, but conversion efficiency ten times higher. In that experiment, an UV ($\lambda = 0.351$ μm) interaction beam was focused on the CH ablator of a multi-layer planar target after plasma-creation beams of lower intensity. The parameters of the interaction beam were similar to our case: 1-ns square pulse $23°$ off the target normal, for a vacuum intensity of $\sim 10^{16}$ W/cm^2. The plasma was characterized by a scale length of $\sim$330 μm and a coronal electronic temperature of 1.8 keV. The difference in the conversion efficiencies between the two experiments could be due to the influence of longer plasma scale-lengths on the LPIs. The behaviour of the LPIs in presence of high values of L_n, relevant to SI scheme, is an open problem currently under investigation [36].
Low HE temperatures of ~ 30 keV are also reported in spherical configuration experiments [37]. In this case, 40 of the 60 OMEGA beams were used to compress D$_2$ filled plastic shells. The remaining 20 spike beams were delayed and tightly focused onto shell to deliver a late shock. The intensity of the single spike beam was several 10^{15} W/cm^2, interacting with a plasma characterized by $L_n \sim$170 μm and T$_e \sim$2 keV. As such, we can observe that the HE temperature does not depend on laser intensity, in agreement with recent theoretical expectations (see for instance [38]). On the contrary, higher temperatures were found in experiments in which different laser beams were overlapped during the interaction [39][40]. These experiments were characterized by longer scale-lengths ($L_n \sim$ 350 - 400 μm) but lower laser intensities ($\sim 10^{15}$ W/cm^2, 1 - 7$\cdot 10^{14}$ W/cm^2 respectively).

Shock characteristic

Fig. 24 shows the temporal progression of different hydrodynamic quantities around the shock front. Results from simulations with and without hot-electrons are presented. The Ablation pressure reaches a maximum of 100 MBar at 0.3 ns for the two cases, regardless of the presence of the hot-electron beam. These values are four times less compared to the value of $\sim$400 MBar predicted by the scaling laws $p_{abl} \propto \lambda^{-2/3} I_a^{2/3}$, observed for laser intensities of 10^{15}W/cm^2 [41]. This mismatch is due to the fact that the scaling law considers 1-D collisional laser absorption without parametric instabilities and non-thermal electrons. Despite this, the obtained values of ablation pressure are in agreement with other planar configurations experiments [2], [39].
Considering that 175 μm of cold plastic stops electrons up to 100 keV, it is possible to estimate that 98% of electrons in the experiment are stopped in the ablator. This increases the electronic temperature and pressure reached by the ablator 50 μm upstream of the shock, 9 eV and 11 MBar, respectively. The downstream pressure reaches a maximum of 150 MBar, 25 MBar more then without HEs. This effect, driven by the presence of electrons, is beneficial for the SI scheme. The shock strength, which is the ratio between the downstream and the upstream pressures at the shock front, decreases dramatically from $\sim$700 for the case without HE to $\sim$20 for the simulations with HE. The shock velocity in presence of HEs increases from 100 km/s to 130 km/s.
Let's notice that low-hot electron temperatures, as those measured in the experiment, will represent an advantage for the SI scheme. The majority of them can be stopped in the ablator, avoiding their penetration into the compressed shell. However, it is important to study the effects of the high energy tail of the distribution (i.e > 100 keV) on the shell and on the hot-spot. These electrons could pre-heat and ablate the cryogenic shell, increasing the hot-spot mass with a detrimental effect.
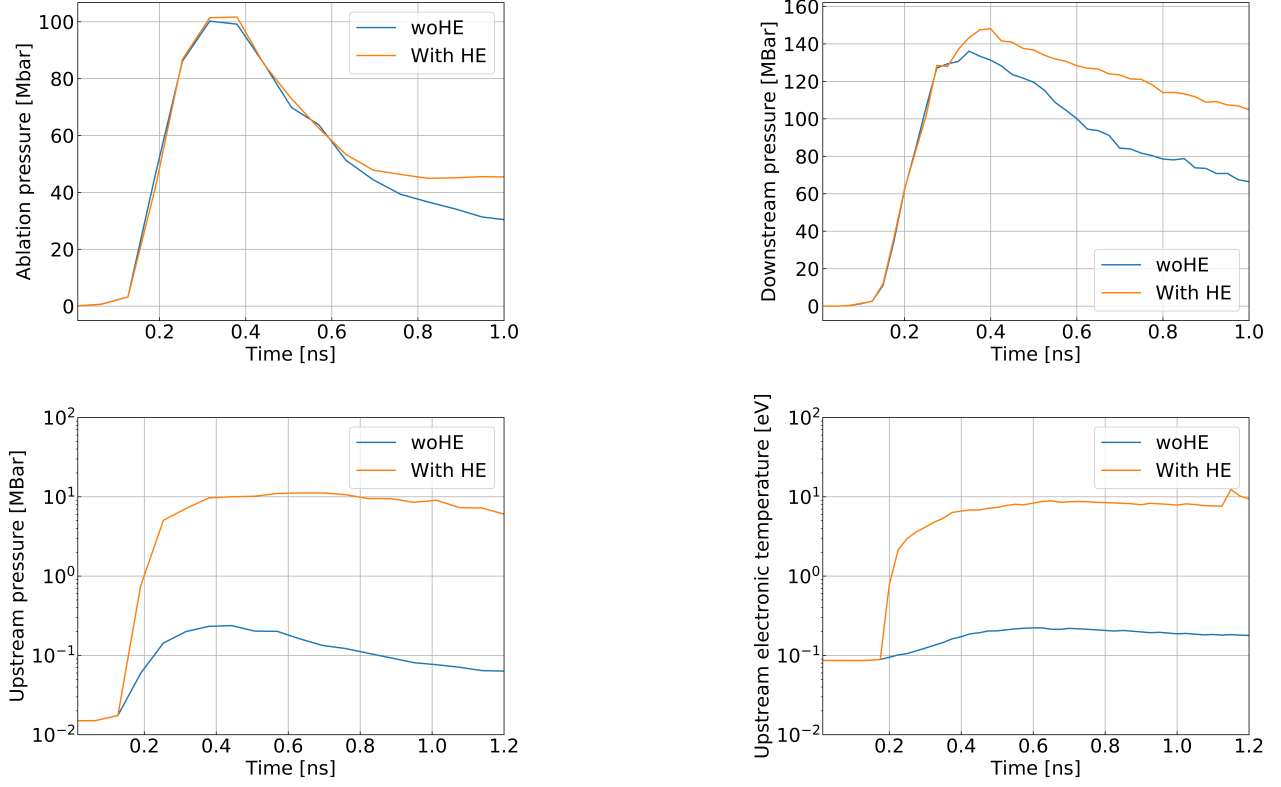
FIG. 24: Evolution in time of hydrodynamic quantities around the shock position resulting from CHIC simulations. The simulation with HE (orange) and without HE (blue) are reported. [Top-Left] Ablation pressure; [Top right] downstream pressure; [Bottom-left] upstream pressure; [Bottom-right] upstream electronic temperature.

SUMMARY AND CONCLUSIONS

Planar multilayer targets (CH 175 μm - Cu 20 μm) were irradiated with UV ($\lambda = 351$ nm) laser pulses at SI-relevant intensities ($\sim 10^{16}$W/cm^2). The plasma scale-length and the coronal temperature computed at $n_c/4$ rised up to 150 μm and 2.1 keV respectively. Two additional laser beams were focused on V foil to produce He$_\alpha$ x-rays to perform 2D time-gated and 1D time-resolved radiographies. The hot-electron population generated in the interaction is characterized in terms of intensity and temperature using different spectrometers. Two time-integrating hard x-ray spectrometers (BMXSs) were used to detect the bremsstrahlung radiation. Zinc von Hamos (ZnVH) and high-resolving-power (HRS) x-ray spectrometers were used to collet K$_\alpha$ signal coming from the transit of electrons in the copper tracer.

The interpretation and the post-processing of spectrometer data (BMXS and ZNVH) are based on MC methods, in which the 3D geometry of the target is reproduced and the response of the spectrometers is simulated. This procedure can be considered appropriate for a first-order interpretation of the results, even if the MC code does not account for the hydrodynamic evolution of the irra-

diated target. The interval of temperature indicated by the spectrometers ranges from 20 keV up to 50 keV, with an energy conversion efficiency that goes from 2% up to 13%. These data are used as input of hydrodynamic simulations reproducing the propagation of the shock in the target and expansion of the Cu layer observed in the radiographies. In this regard, hydrodynamic simulations suggest that lower values of temperatures (T$_h$ = 27 keV $\pm$7 keV) and higher conversion efficiencies (η = 10% $\pm$4%) are more appropriate. The simulation with HE beam with these parameters predicts a copper heating at the end of laser pulse in agreement with the temperature which can be inferred from the broadening of the K$_\alpha$ line as measured by the HRS spectrometer.

In our experiment, HE are found to increase the downstream pressure from about 125 to 150 MBar and the shock velocity from 100 km/s to 130 km/s. On the other side, the deposition of energy upstream of the shock increases the pressure of the ablator, resulting in a dramatic decrease of the shock strength.

To conclude, the low HE temperature and high conversion efficiency which we have measured are quite a good news for SI, since the majority of the HE will not be able to penetrate deeply into the compressed fuel and there-

fore might even result in a positive factor in full-scale SI experiments.

ACKNOWLEDGMENT

---

* alessandro.tentori@u-bordeaux.fr

[1] R. Betti, C. D. Zhou, K. S. Anderson, L. J. Perkins, W. Theobald, and A. A. Solodov, Phys. Rev. Lett. **98**, 155001 (2007).

[2] D. Batani, S. Baton, A. Casner, S. Depierreux, M. Hohenberger, O. Klimo, M. Koenig, C. Labaune, X. Ribeyre, C. Rousseaux, G. Schurtz, W. Theobald, and V. Tikhonchuk, Nuclear Fusion **54**, 054009 (2014).

[3] D. W. Forslund, J. M. Kindel, and E. L. Lindman, The Physics of Fluids **18**, 1002 (1975).

[4] *The physics of Laser Plasma Interactions* (Frontiers in Physics Series, 1985).

[5] A. Colatis, X. Ribeyre, E. Le Bel, G. Duchateau, P. Nicola, and V. Tikhonchuk, Physics of Plasmas **23**, 072703 (2016).

[6] S. Gus'kov, X. Ribeyre, M. Touati, J.-L. Feugeas, P. Nicolaï, and V. Tikhonchuk, Phys. Rev. Lett. **109**, 255004 (2012).

[7] L. Antonelli, J. Trela, F. Barbato, G. Boutoux, P. Nicola, D. Batani, V. Tikhonchuk, D. Mancelli, A. Tentori, S. Atzeni, A. Schiavi, F. Baffigi, G. Cristoforetti, S. Vi-

ciani, L. A. Gizzi, M. Smid, O. Renner, J. Dostal, R. Dudzak, L. Juha, and M. Krus, Physics of Plasmas **26**, 112708 (2019), https://doi.org/10.1063/1.5119697.

[8] D. Batani, L. Antonelli, F. Barbato, G. Boutoux, A. Colatis, J.-L. Feugeas, G. Folpini, D. Mancelli, P. Nicolai, J. Santos, J. Trela, V. Tikhonchuk, J. Badziak, T. Chodukowski, K. Jakubowska, Z. Kalinowska, T. Pisarczyk, M. Rosinski, M. Sawicka, F. Baffigi, G. Cristoforetti, F. D'Amato, P. Koester, L. Gizzi, S. Viciani, S. Atzeni, A. Schiavi, M. Skoric, S. Gus'kov, J. Honrubia, J. Limpouch, O. Klimo, J. Skala, Y. Gu, E. Krousky, O. Renner, M. Smid, S. Weber, R. Dudzak, M. Krus, and J. Ullschmied, Nuclear Fusion **59**, 032012 (2018).

[9] L. Waxer, D. Maywar, J. Kelly, T. Kessler, B. Kruschwitz, S. Loucks, R. McCrory, D. Meyerhofer, S. Morse, C. Stoeckl, and J. Zuegel, Opt. Photon. News **16**, 30 (2005).

[10] L. C. Jarrott, M. S. Wei, C. McGuffey, F. N. Beg, P. M. Nilson, C. Sorce, C. Stoeckl, W. Theoboald, H. Sawada, R. B. Stephens, P. K. Patel, H. S. McLean, O. L. Landen, S. H. Glenzer, and T. Dppner, Review of Scientific Instruments **88**, 043110 (2017), https://doi.org/10.1063/1.4981793.

[11] P. M. Nilson, F. Ehrne, C. Mileham, D. Mastrosimone, R. K. Jungquist, C. Taylor, C. R. Stillman, S. T. Ivancic, R. Boni, J. Hassett, D. J. Lonobile, R. W. Kidder, M. J. Shoup, A. A. Solodov, C. Stoeckl, W. Theobald, D. H. Froula, K. W. Hill, L. Gao, M. Bitter, P. Efthimion, and D. D. Meyerhofer, Review of Scientific Instruments **87**, 11D504 (2016).

[12] C. D. Chen, J. A. King, M. H. Key, K. U. Akli, F. N. Beg, H. Chen, R. R. Freeman, A. Link, A. J. Mackinnon, A. G. MacPhee, P. K. Patel, M. Porkolab, R. B. Stephens, and L. D. Van Woerkom, Review of Scientific Instruments **79**, 10E305 (2008).

[13] T. J. Kessler, Y. Lin, J. J. Armstrong, and B. Velazquez, in *Laser Coherence Control: Technology and Applications*, Vol. 1870, edited by H. T. Powell and T. J. Kessler, International Society for Optics and Photonics (SPIE, 1993) pp. 95 – 104.

[14] D. K. Bradley, P. M. Bell, J. D. Kilkenny, R. Hanks, O. Landen, P. A. Jaanimagi, P. W. McKenty, and C. P. Verdon, Review of Scientific Instruments **63**, 4813 (1992), https://doi.org/10.1063/1.1143571.

[15] O. V. Gotchev, P. A. Jaanimagi, J. P. Knauer, F. J. Marshall, and D. D. Meyerhofer, Review of Scientific Instruments **75**, 4063 (2004), https://doi.org/10.1063/1.1786649.

[16] A. Curcio, P. Andreoli, M. Cipriani, G. Claps, F. Consoli, G. Cristofari, R. De Angelis, D. Giulietti, F. Ingenito, and P. D., Journal of Instrumentation **11**, C05011 (2016).

[17] G. Boutoux, D. Batani, F. Burgy, J. Ducret, P. Forestier-Colleoni, S. Hulin, N. Rabhi, A. Duval, L. Lecherbourg, C. Reverdin, K. Jakubowska, C. Szabo, S. Bastiani-Ceccotti, F. Consoli, A. Curcio, R. De angelis, F. Ingenito, J. Baggio, and D. Raffestin, Review of Scientific Instruments **87** (2016), 10.1063/1.4944863.

[18] S. Agostinelli *et al.* (GEANT4), Nucl. Instrum. Meth. A **506**, 250 (2003).

[19] Salvat, *PENELOPE: A code system for Monte Carlo simulation of electron and photon transport* (Nuclear Energy Agency, 2019).

[20] S. Pucella, *Fisica dei plasmi* (Zanichelli, 2014).

[21] S. T. Perkins, D. E. Cullen, M. H. Chen, J. Rathkopf, J. Scofield, and J. H. Hubbell, (1991), 10.2172/10121422.

[22] X. Llovet, C. Powell, F. Salvat, and A. Jablonski, Journal of Physical and Chemical Reference Data **43** (2014), 10.1063/1.4832851.

[23] M. P. Breil J., Galera S., Computers and Fluids **46** (2011), https://doi.org/10.1016/j.compfluid.2010.06.017, 10th ICFD Conference Series on Numerical Methods for Fluid Dynamics (ICFD 2010).

[24] J. F. Myatt, J. G. Shaw, R. K. Follett, D. H. Edgell, D. H. Froula, J. P. Palastro, and V. N. Goncharov, Journal of Computational Physics **399**, 108916 (2019).

[25] A. Colaitis, *Multiscale description of the laser-plasma interaction: application to the physics of shock ignition in inertial confinement fusion*, Ph.D. thesis, SPI Université de Bordeaux (2015).

[26] A. A. Solodov and R. Betti, Physics of Plasmas **15**, 042707 (2008), https://aip.scitation.org/doi/pdf/10.1063/1.2903890.

[27] R. M. More, *Plasma processes in non-ideal plasmas*, Tech. Rep. (LLNL, 1985) 29th Scottish Universities Sumner School in Physics "Laser Plasma Interactions" 1985.

[28] C. Li and R. Petrasso, Physical review. E, Statistical, nonlinear, and soft matter physics **73**, 016402 (2006).

[29] D. Watteau, *La fusion thermonuclaire inertielle par laser: linteraction laser-matire part. 1, vol. 1. (French Edition)*, edited by CEA (CEA, 1991).

[30] A. Colatis, G. Duchateau, X. Ribeyre, Y. Maheut, G. Boutoux, L. Antonelli, P. Nicolai, D. Batani, and V. Tikhonchuk, Phys. Rev. E **92**, 041101 (2015).

[31] J. Trela, *Effect of hot-electrons on the hydrodynamic of shocks and implosions for shock ignition*, Ph.D. thesis, SPI Université de Bordeaux (2019).

[32] P. Palmeri, G. Boutoux, D. Batani, and P. Quinet, Phys. Rev. E **92**, 033108 (2015).

[33] J. J. MacFarlane, I. E. Golovkin, P. Wang, P. R. Woodruff, and N. A. Pereyra, High Energy Density Physics **3**, 181 (2007).

[34] B. B. Afeyan and E. A. Williams, The Physics of Fluids **28**, 3397 (1985), https://aip.scitation.org/doi/pdf/10.1063/1.865340.

[35] S. Zhang, C. Krauland, J. Peebles, J. Li, F. Beg, N. Alexander, W. Theobald, R. Betti, D. Haberberger, M. Campbell, R. Yan, E. Borwick, C. Ren, and M. Wei, Physics of Plasmas **27**, 023111 (2020).

[36] S. Baton, A. Colatis, C. Rousseaux, G. Boutoux, S. Brygoo, L. Jacquet, M. Koenig, D. Batani, A. Casner, E. L. Bel, D. Raffestin, A. Tentori, V. Tikhonchuk, J. Trela, C. Reverdin, L. Le-Deroff, W. Theobald, G. Cristoforetti, L. Gizzi, P. Koester, L. Labate, and K. Shigemori, High Energy Density Physics **36**, 100796 (2020).

[37] W. Theobald, R. Nora, M. Lafon, A. Casner, X. Ribeyre, K. Anderson, R. Betti, J. Delettrez, J. Frenje, V. Glebov, O. Gotchev, M. Hohenberger, S. Hu, F. Marshall, D. Meyerhofer, T. Sangster, G. Schurtz, W. Seka, V. Smalyuk, and B. Yaakobi, Physics of Plasmas **19**, 16 (2012).

[38] O. Klimo, V. T. Tikhonchuk, X. Ribeyre, G. Schurtz, C. Riconda, S. Weber, and J. Limpouch, Physics of Plasmas **18**, 082709 (2011), https://doi.org/10.1063/1.3625264.

[39] M. Hohenberger, W. Theobald, S. X. Hu, K. S. Anderson, R. Betti, T. R. Boehly, A. Casner, D. E. Fratanduono, M. Lafon, D. D. Meyerhofer, R. Nora, X. Ribeyre, T. C. Sangster, G. Schurtz, W. Seka, C. Stoeckl, and B. Yaakobi, Physics of Plasmas **21**, 022702 (2014), https://doi.org/10.1063/1.4865373.

[40] B. Yaakobi, P.-Y. Chang, A. Solodov, C. Stoeckl, D. Edgell, S. Craxton, S. Hu, J. Myatt, F. Marshall, W. Seka, and D. Froula, Physics of Plasmas **19** (2012), 10.1063/1.3676153.

[41] J. Lindl, Physics of Plasmas **2**, 3933 (1995), https://doi.org/10.1063/1.871025.